# How fine particles alter wave propagation in granular media: insights from micromechanical modelling

X. TANG\* and J. YANG\*

This paper presents an attempt to address an intriguing question about the role of fine particles in altering wave propagation in granular media from the micromechanical perspective. A special effort is made to examine whether the state dependency of shear wave velocity can be characterised in a unified manner and to establish micromechanical understanding of the observations from recent physical experiments. To simulate the wave propagation accurately, several novel techniques are used to build the numerical model to a scale comparable to laboratory specimens and to effectively eliminate the near-field effect and boundary reflections. It is shown that, with the presence of fines, the degradation of elastic wave velocity is directly associated with the reduction of coordination number. The dispersion relationship constructed from the space—time data of all particles reveals that even a small quantity of fines can cause severe frequency filtering and attenuation. In association with recent experimental work, the unified method of characterising the shear wave velocity by the state parameter in the critical state theory is confirmed by the simulations of both small-strain wave propagation and large-strain triaxial compression tests. At the microscopic level, a sound relationship is found between the mechanical coordination number and the stress-normalised shear wave velocity.

KEYWORDS: discrete element method; dispersion; fines content; granular materials; micromechanics; numerical simulations; small strain stiffness; wave propagation

### INTRODUCTION

The presence of fine particles in natural and synthetic granular materials has been recognised as a critical role in determining the mechanical responses, and how to understand and characterise the effect is emerging as an active area of research across disciplines. An essential block of current knowledge is built on extensive laboratory experiments, from evaluating the liquefaction susceptibility of sands (Kuerbis et al., 1988; Žlatović & Ishihara, 1995; Lade & Yamamuro, 1997; Murthy et al., 2007; Yang & Wei, 2012) to characterising their small-strain stiffness (Salgado et al., 2000; Chien & Oh, 2002; Wichtmann et al., 2015; Yang & Liu, 2016) in geomechanics and earthquake engineering. To illustrate this, the accurate measurement of shear wave velocity  $(V_s)$  and the associated small-strain shear modulus  $(G_0)$  are mainly obtained through dynamic probing techniques, among which the piezoelectric bender element has been frequently used to generate elastic waves and yield propagation velocities. The great compatibility of bender elements makes them quite practical and efficient tools, together with common laboratory testing apparatuses (i.e. oedometer, triaxial cell and resonant column). However, as the database grows rapidly from bender elements, concerns also become increasingly apparent when analysing and interpreting different results, even for a very close topic. On the one hand, it has to be realised that the versatility of the bender element has also created different testing setups as well as signal interpretation techniques accordingly,

which makes the comparison of results impractical. For instance, after summarising the test data of international parallel tests for small-strain shear modulus, it was found that the scatter of results points could be attributed to either the sample preparation procedures or the arrival time identifications (Yamashita et al., 2009; Yang & Gu, 2013). On the other hand, a comprehensive testing programme is costly and time-consuming, since the fines, as another influencing factor in addition to void ratio and stress levels, can vary in size, shape and even plasticity (Yang & Wei, 2012; Wei & Yang, 2014). Recently, laboratory experiments have been performed to study ultrasound transmission through granular media using advanced technologies such as X-ray tomography (Zhai et al., 2020). It can be quite useful to understand wave propagation based on the information of imaged particulate media rather than a black box. However, these tests are currently often limited in terms of grain diameter and sample size.

The discrete-element method (DEM) is designed to simulate the interactions by contact laws and kinetics by Newton's second law of distinct particles. With increasing capabilities, DEM has been approved to be ideal for micromechanical investigations into a series of challenging problems in geophysics and geotechnics (Cundall & Strack, 1979; Oda, 1982; Tsuji et al., 1993; Gu et al., 2020; Zunker & Kamrin, 2024). With regard to modelling wave propagation, a limited number of attempts have shown great potential to overcome some of the limitations in the laboratory and contributed to improvement of our understanding. A good example can be found from the numerical investigation of whether the small-strain modulus is grain size dependent (Ning et al., 2015), which was intended to examine the original finding from well-controlled laboratory tests (Yang & Gu, 2013). The DEM results from wave propagation simulation made the conclusion more persuasive through extending the range limit of particle size from 2.0 mm to 200.0 mm, which is almost impossible in any

Manuscript received 28 August 2024; revised manuscript accepted 30 December 2024. First published online ahead of print 6 January 2025.

<sup>\*</sup> Department of Civil Engineering, The University of Hong Kong, Hong Kong.

common laboratory setting. Although it is difficult to physically prepare granular specimens with precisely determined roughness, the surface roughness was incorporated into Hertzian contact law in DEM and the effect of roughness on the small-strain shear modulus was examined, especially at low confining pressures (Otsubo et al., 2017). The numerical techniques on modelling propagation have been continuously evolving to improve reliability and functionality. Similarly to the physical test setting in Jia (2004), an attempt was made to examine how different damping ratios affect the coherent and coda-like parts of waveforms through a two-dimensional (2D) DEM model (Somfai et al., 2005). To mimic the bender element tests, the wave propagation process was simulated by agitating a single particle where the near-field effect was detected and analysed from a series of three-dimensional (3D) screenshots (O'Donovan et al., 2015).

It should be noted, however, that simulating wave propagation in a sample of representative volume element (RVE) size usually focuses on extracting elastic wave velocities from time-domain signals where the near-field effect is still possibly pronounced. In terms of sample size, there was a study that showed the elastic wave velocities depend on the positions of receivers along the entire granular bar and revealed that even slight disorder into regular packing can cause noticeable frequency filtering (Mouraille & Luding, 2008). In a subsequent study, the differences were spotted in the results obtained for small-strain stiffness in relation to static compression and wave propagation tests (Cheng et al., 2020). With elongated granular specimens, they demonstrated that the peak branch of the dispersion relation can provide the most consistent results of elastic wave velocities regardless of input frequencies. More recently, a scaled-up DEM model was built to simulate the wave propagation in granular assemblies with different shape factors (Tang & Yang, 2021), which confirmed laboratory experimental results that the wave velocity increases with particle angularity (Liu & Yang, 2018). Therefore, it can be beneficial to adopt the most updated modelling techniques to simulate the wave propagation in granular media containing fines in order to deepen our understanding of this important problem.

As fines content (FC) varies from case to case either in the laboratory or on site, it is essential to characterise the effect of fines in predicting  $V_s$  and  $G_0$  for a broad range of engineering applications. The void ratio and confining stress are considered as key factors that can be expressed as:

$$G_0 = AF(e) \left(\frac{p}{p_a}\right)^n \tag{1}$$

where  $G_0$  is in MPa; p is the mean effective stress in kPa;  $p_a$ is a reference stress (i.e. 101 kPa); A and n are two best-fit parameters; and F(e) is an empirically defined function of current void ratio e (i.e. the void ratio corresponding to the mean effective stress p). It can be expected that numerous sets of A and n will be identified as long as FC changes. One of the possible methods is to incorporate the variant FC into existing parameters. For instance, an empirical model was proposed to transform the effect of gradation and FC into void ratio function F(e) and stress exponent n (Wichtmann et al., 2015). Nonetheless, the eventual function becomes cumbersome and has potential limitation for materials outside the database. As reported, the liquefaction potential notably increases as crushed silica silt is added into Toyoura sand, which clearly indicates that the shear behaviour of granular materials is state dependent (Yang & Wei, 2012). In a following study by Yang & Liu

(2016), both resonant column and bender element tests were conducted over a series of mixtures of clean quartz sand and crushed silica fines; based on the physical observations that  $G_0$  decreases as the FC increases, an alternative method was proposed to characterise  $G_0$  for both clean sand and sand–fines mixtures using the state parameter ( $\Psi$ ) in the context of critical state theory (Been & Jefferies, 1985). Later, an appealing framework was proposed to evaluate the state of sand with varying FC by  $V_s$  (Yang et al., 2018). As the framework is built on two types of laboratory experiments at small strain and large strain, it is of great interest to examine whether it can be validated by the particle-level simulations and, more importantly, what is the micromechanical mechanism involved.

This paper presents an attempt to address these concerns with the aim to develop new insights into the behaviour of wave propagation in granular media containing fines. The structure of this paper is as follows. First, the numerical techniques and procedures are introduced for small-strain elastic wave propagation and large-strain triaxial tests that are both performed. Second, specific simulation cases are prepared to demonstrate the effect of FC on wave propagation along with interpretation and analysis on wave speed, attenuation and frequency filtering. The general trend of wave velocities with varying FC and the micromechanical analysis will then be presented. Finally, the unified method of characterising wave velocities by state parameter, developed from recent experimental results (Yang et al., 2018), is examined using the systematic dataset from both smallstrain and large-strain simulations, and the underlying micromechanical mechanism is explored.

#### NUMERICAL MODELLING

The DEM simulations are performed using the in-house numerical code developed on the platform of LIGGGHTS (Kloss *et al.*, 2012) and parallel computing resources from the University of Hong Kong are leveraged to complete several hundreds of simulation cases used in the current study.

Test material and sample preparation

The material includes two parts to mimic laboratory experiments: coarse particles as the base material and fine particles as the additive. The base material has a mean particle size of  $1.0 \,\mathrm{mm}$  with the coefficient of uniformity  $C_u$  of 1.53. The fine particles have the mono size of 0.286 mm and are mixed with the base material counted by weight, namely, FC = 0, 2.5, 5.0 and 10%. The size ratio (SR),  $D_{50}/d_{50}$ , is approximately 3.50, where  $D_{50}$  and  $d_{50}$  are the mean sizes of base material and FC, respectively. The resulting grading curves are plotted in Fig. 1 and the assemblies with varying FC are abbreviated as FC-0, FC-2.5, FC-5 and FC-10, respectively. The value of SR is essential for bimodal or gap-graded packings where fines can exist in the voids formed by coarse grains (Lade et al., 1998; Rahman & Lo, 2008; Yang et al., 2015; Shire & O'Sullivan, 2016; Wei & Yang, 2023). In this study, the SR between coarse and fine particles is selected so that the role of fines can be investigated at reasonable computation cost. Laboratory tests have shown that the effect of fines is evident on elastic wave velocity and associated modulus at SR values of 3.5 (Choo & Burns, 2015) and 4.0 (Yang & Liu, 2016). With regard to particle-level simulations, Liu et al. (2023) showed that the trapping effect of fines between coarse particles is observed when SR = 3.7 and  $FC \le 20\%$ . The numbers of coarse and fine particles in this study are

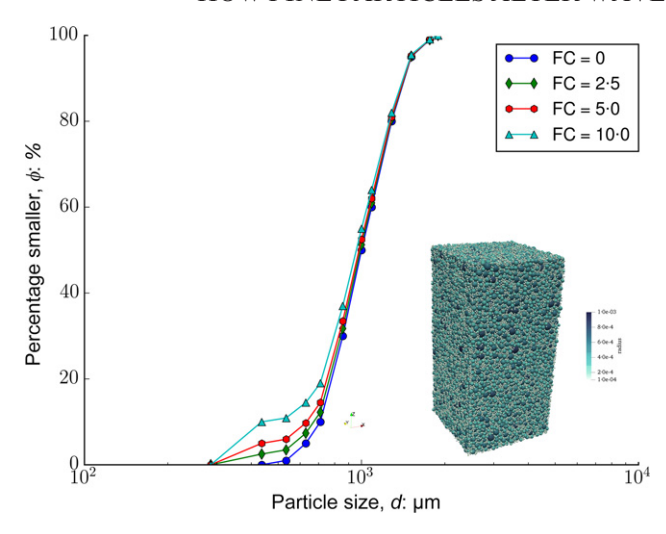


Fig. 1. Particle size distribution curves with inset plot of FC-10 RVE at 50 kPa.

summarised in Table 1. The interparticle forces between contact objects can be calculated based on force—displacement law in normal and shear directions (Johnson, 1985). Similarly to other geomechanical modelling, here the nonlinear Hertz—Mindlin contact law is adopted for all particles. With the normal overlap  $\delta_n$  and the relative tangential displacement  $\delta_t$ , the normal and shear contact forces,  $f_n$  and  $f_t$ , are obtained based on the force—displacement law as (Tang & Yang, 2021):

$$f_n = k_n \delta_n = \frac{4}{3} E^* \sqrt{R^* \delta_n} \delta_n \tag{2}$$

$$\Delta \mathbf{f}_t = k_t \Delta \mathbf{\delta}_t = 8G^* \sqrt{R^* \mathbf{\delta}_n} \ \Delta \mathbf{\delta}_t \tag{3}$$

$$|f_t| \le \tan \mu |f_n| \tag{4}$$

with

$$\frac{1}{E^*} = \frac{\left(1 - \nu_i^2\right)}{E_i} + \frac{\left(1 - \nu_j^2\right)}{E_j}$$

$$\frac{1}{G^*} = \frac{2(2 - \nu_i)(1 + \nu_j)}{E_i} + \frac{2(2 - \nu_j)(1 + \nu_i)}{E_j}$$

$$\frac{1}{R^*} = \frac{1}{R_i} + \frac{1}{R_j}$$

where substitutes i and j represent the two contacting particles; E and v are the Young's modulus and Poisson's ratio of particles; R refers to the particle radius; and  $\mu$  is the interparticle friction coefficient. It is obvious that the tangential force  $f_i$  needs to be updated and calculated in an incremental

manner at each time step and checked against its maximum  $f_l$ . The material properties are selected for typical quartz: Young's modulus is 70 GPa, the Poisson's ratio is 0·22 and the interparticle friction coefficient is 0·25 unless otherwise specified (Huang *et al.*, 2014). In the case where sand particles and fines have significantly different mineral compositions, then different material properties can be assumed for sand and fine particles. Throughout the study, periodic boundary conditions are always maintained. To make each RVE, non-contact spheres including fine grains are initially placed into the periodic cell with the dimensions slightly larger than  $19 \times 19 \times 38 \text{ mm}^3$  (hereafter length by width by height or *X*-axis by *Y*-axis by *Z*-axis). The average stress tensor follows the formula (Christoffersen *et al.*, 1981):

$$\boldsymbol{\sigma} = \frac{1}{V} \sum_{N_c} \boldsymbol{f}^c \otimes \boldsymbol{d}^c \tag{5}$$

where  $N_c$  refers to the total contact number; V is the cell volume;  $d^c$  is the branch vector joining two centroids of particles; and  $f^c$  is the contact force. And the average strain tensor is simply calculated from the cell deformation:

$$\varepsilon_i = \frac{H_i(t) - H_i(t_0)}{H_i(t_0)} \tag{6}$$

where  $H_i(t)$  and  $H_i(t_0)$  are the cell dimensions at current and reference configuration, respectively. Then the periodic cell is subjected to isotropic consolidation through a stress-controlled servo system (Cundall, 1988):

$$\dot{\varepsilon} = \dot{\varepsilon}_{max} \frac{\sigma_{tar} - \sigma_{cur}}{\sigma_{tar}} \tag{7}$$

where  $\dot{\epsilon}_{max}$  is the input parameter that regulates the largest strain rate at every time step;  $\sigma_{tar}$  and  $\sigma_{cur}$  denote the target stress and current stress level, respectively. The consolidation process will terminate only when the stress tolerance is stably below 0·001%, during which the local damping coefficient is set as 0·1 (Cundall & Strack, 1979) and will be adjusted to 0 during the wave tests. Using different inter-particle friction coefficients (i.e. from 0 to 0·25), in total, 185 granular specimens are generated with varying initial density under the isotropic confining pressure of 50 kPa. The initial RVEs will then be isotropically compressed to the target stress levels (i.e. 100 to 5000 kPa) for the following numerical tests.

# Triaxial test simulation

Often in laboratory experiments, triaxial tests and wave propagation tests are performed separately on different specimens. In this study, the isotropically consolidated RVEs used for the wave propagation tests will be subjected to triaxial tests to establish critical state parameters. This approach allows for reducing the possible uncertainties from physical tests and obtaining more accurate critical state parameters for the interpretation of wave velocities in the critical state framework. With RVEs at varying initial states, different types of triaxial tests are simulated under a dry

Table 1. Number of base materials and fines particles in RVEs and elongated specimens with varying FC

Number of particles	FC-0	FC-2·5	FC-5	FC-10
RVE				
Fines content	0	2.5%	5%	10%
Base materials	16 400	16 324	16 150	16433
Fines particles	0	16176	32 850	70 567
Total	16 400	32 500	49 000	87 000
Elongated	•	•		•
Total	131 200	260 000	392 000	696 000

condition including the conventional compression test, constant mean stress compression test and constant volume test. It should be noted again that the current DEM model simulates the dry grains where no fluid pressure is generated. The inertia number and strain level are consistently monitored to obtain reliable mechanical responses. Consistent results on critical state can be obtained if the inertial number,  $\mathcal{L}$ , is below  $1.0 \times 10^{-3}$  during the triaxial test (Lopera Perez *et al.*, 2016). The inertial number is expressed as in (Da Cruz *et al.*, 2005):

$$\mathcal{L} = \dot{\gamma} \bar{d} \sqrt{\frac{\rho_g}{p}} \tag{8}$$

where  $\dot{\gamma}$  is the shearing rate;  $\bar{d}$  is the mean particle size;  $\rho_g$  is the particle density; and p is the mean effective stress. And the critical state of granular soils can be analytically described as:

$$\begin{cases} \dot{p} = 0 \\ \dot{\mathbf{s}} = 0 \\ \dot{\varepsilon}_{v} = 0 \\ \dot{\mathbf{e}}_{d} \neq 0 \end{cases}$$

$$(9)$$

where the superposed dot denotes the incremental quantities; p stands for the hydrostatic pressure in terms of  $p = \frac{1}{3} \text{tr} \sigma$ ; s refers to the deviatoric stress tensor acquired from  $s = \sigma - pI$ ;  $\varepsilon_v = \text{tr}\varepsilon$  stands for the volumetric strain with  $\varepsilon$  as the strain tensor;  $\varepsilon_d = \varepsilon - \frac{\varepsilon_y}{3} I$  stands for the deviatoric strain (Yang & Luo, 2015). The recent anisotropic critical state theory enhances the requirement for reaching the critical state by including a fabric quantity (Li & Dafalias, 2012). It should be noted that fabric and its evolution is difficult to measure in physical experiments as compared with the quantities specified in equation (9). To ensure the attainment of critical states in the simulations, the loading will not be terminated until the axial strain is equal to or higher than 50% (except for the cases with failure). Also, strain localisation (Alshibli et al., 2003) is avoided in the simulations with the aid of periodic boundary conditions.

# Wave propagation simulation

It should be mentioned that the periodic cell is inherently suitable for multiplying the element specimen. Under

periodic boundary conditions, ghost particles are identical from the other side or near the edges or boundaries. In this study, MPI parallel computing is activated so that the particle and kinetic information are stored in each subprocessor during timestep iterations. As illustrated in Fig. 2, the information of a RVE was gathered from the last previous timestep and re-signed to an expanded new sub-domain. In terms of expected dimension, each RVE is replicated by eight times in the Z-axis (Cheng et al., 2020; Tang & Yang, 2021), thus resulting in an elongated sample a little smaller than  $19 \times 19 \times 304$  mm<sup>3</sup>. It is apparent that the height dimension now becomes comparable with physical specimen size in some of the laboratory experiments (Yang & Gu, 2013; Yang & Liu, 2016). The elongated specimen can create enough space for a more complete wave propagation to be clearly observed, captured and analysed. Despite the obvious increase in computation cost, the benefit of increasing sample size can provide information of continuous change of the frequency spectrum. Following the replication process, the calm-down process is necessary and one type of artificial damping is introduced as:

$$\mathbf{f}_{\mathrm{vd}} = -\gamma_{\mathrm{vel}} \|\mathbf{f}^p\| \mathrm{sign}(\mathbf{v}^p \cdot \mathbf{f}^p) \tag{10}$$

where  $f_{\rm vd}$  is the damping force caused by this damping mechanism;  $\gamma_{\text{vel}}$  is the velocity damping coefficient, which falls into [0, 1.0]; v is the current velocity. The calm-down cycles are terminated once the average particle velocity is steadily on or below  $1.0 \times 10^{-7}$  m/s. For numerical modelling of wave propagation, the boundary condition is crucial as the element sample is limited compared to the wave propagation distance, and thus potentially affects simulation accuracy. In the current study, as demonstrated in Fig. 3, boundary conditions are also carefully treated whereby two outermost layers are thoroughly frozen and the immediate neighbouring layers are the cushion layers that absorb kinetic energy based on artificial damping. Except for the frozen boundary layers, the coefficient of restitution  $(C_r^p)$  has been considered for particles to characterise the physical energy dissipation associated with contact impact, and the  $C_{r}^{p}$  value of 0.95 (Gollwitzer et al., 2012) is adopted. Otherwise, none of any artificial damping

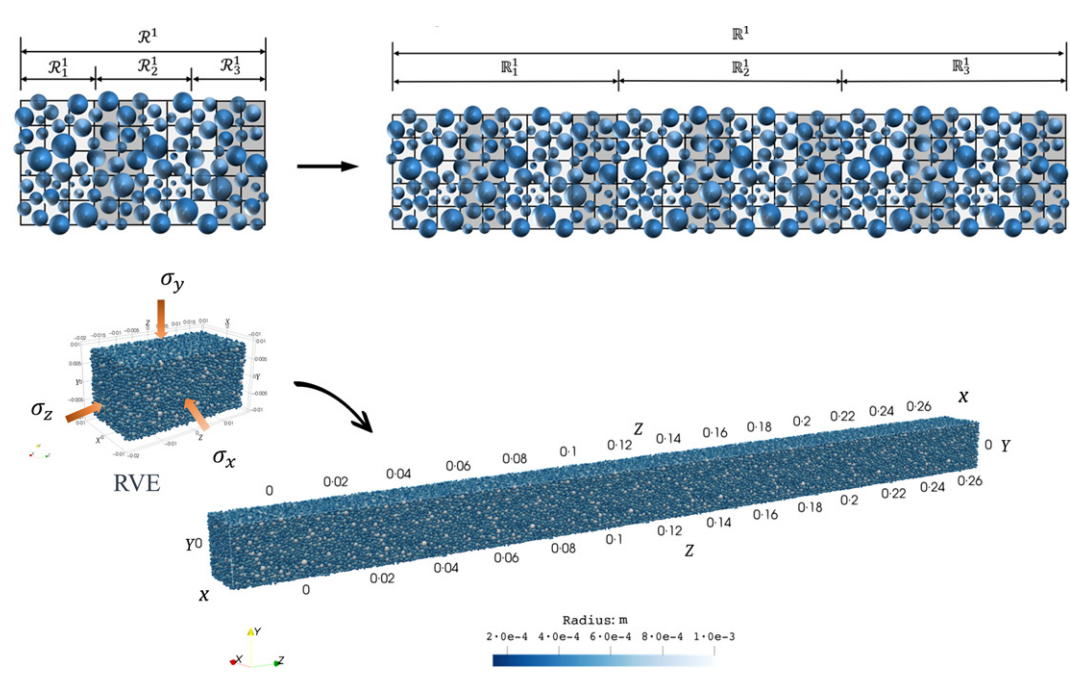


Fig. 2. Illustration of generating elongated sample from representative volume element (RVE) under parallel computing framework

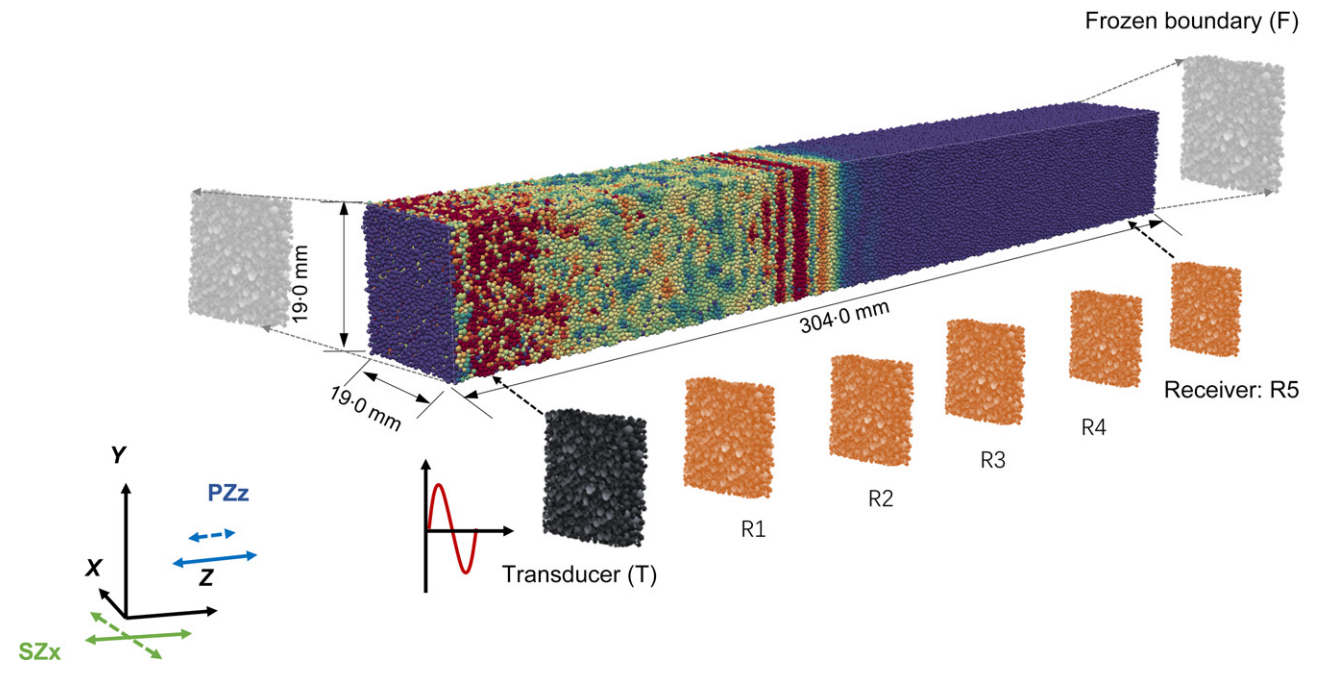


Fig. 3. Illustration of key elements involved in modelling wave propagation in enlarged granular medium. The input wave signal is agitated as a single sine wave with minimum velocity amplitude as the boundary condition treatment

is effective during the wave propagation test. In this way, a wave can propagate from one end towards another with very minimal reflections and disturbance; more details can be found in Tang & Yang (2021). The elastic wave is agitated by way of a transmitter in the form of velocity at  $1.0 \times 10^{-3}$  m/s, which causes the maximum displacement below  $1.0 \times 10^{-8}$  m and thus preserves the very small-strain regime. Then the wave will propagate towards the other end with minimal reflections and with periodicity in the other two directions. It is noted that the input waveform is taken as a single sine wave:

$$\mathbf{v} = \mathbf{v}_0 + A\sin\left(\omega t\right) \tag{11}$$

where the A is the amplitude in terms of velocity;  $\omega = 2\pi f$  is the input angular frequency and f is the frequency;  $v_0$  is the original velocity that is at or below  $1.0 \times 10^{-7}$  m/s. The input frequencies ( $f_{in}$ ) are selected from 10 kHz to 400 kHz as the wavelength helps to avoid the near-field effect without losing the wave signal quality. The input parameters are summarised in Table 2. The input frequency used to be a major issue in the physical test as it couples with the effect

Table 2. Key input parameters for the current numerical model

Terms	Value	Unit
Dimension of RVE Dimension of long sample	$19 \times 19 \times 38$ $19 \times 19 \times 304$	mm <sup>3</sup>
Mean particle size of base material, $D_{50}$	1.0	mm
Mean particle size of fines, $d_{50}$ Particle Young's modulus, $E_p$	0·286 70·0	mm GPa
Particle Poisson's ratio, $v_p$ Particle restitution coefficient, $C_r^p$	0·22 0·95	_
Consolidation inter-particle friction, $\mu_{cons}$ Shear inter-particle friction, $\mu_{shear}$	0.0 to 0.2475 0.25	_
Input sine wave amplitude, $A_{in}$	$1.0 \times 10^{-3}$ 10 to 400	m/s kHz
Input sine wave frequency, $f_{in}$ Time step, $\Delta t$	$5.0 \times 10^{-9}$	S S
Local damping coefficient, $\gamma_{local}$	0·1 (0 during wave test)	_
Velocity damping coefficient, $\gamma_{\text{vel}}$	0.5 (0 during wave test)	_

from sample size and grain size. As illustrated in Fig. 3, there are five evenly distributed distances between the transducer (T) and receiver no. 5 (R5). For a given specimen, the relative positions of all receivers are so assigned and fixed in this manner once the elongation process is completed. As shown in Fig. 4, the variation of input frequencies (10 to 400 kHz) is observed to affect the forms of received signals. The peak amplitude of the received signal decreases as the input frequency increases. The peak-topeak method is commonly applied to sine wave input, where the travel time is defined as the difference between the peak of the input signal and the first corresponding peak of the output signal. For example, in Fig. 4, the travel time and wave velocity at R2 can be determined sequentially with increasing input frequency. It turns out that the calculated speeds are almost identical and the effect of input frequency is very minor.

### Interpretation of wave signals

For a common wave experiment, the input waveform and detected waveform are the only key information with certain propagation distances. Even so, the determination of the wave velocity from physical tests usually faces many uncertainties and a unified technique is quite challenging. Therefore, multiple receivers are placed along the propagation direction to examine if the determined propagation speed is consistent (i.e. abbreviated as R1 to R5 in Fig. 3). Based on the preliminary findings, the peak-to-peak method is selected to determine the so-called time-of-flight velocity of the specimen with  $f_{in} = 100$  kHz, which gives very consistent results; a similar observation was noted in Cheng et al. (2020). Taking advantage of the DEM, it is convenient to monitor and record the kinetic information of every particle during every timestep of the propagation process. The dispersion relation is therefore generated by 2D Fourier transformation (Mouraille & Luding, 2008; Saitoh et al., 2019). For any particle inside the long sample, its position can be expressed as  $x_i$  and the velocity evolution with time as  $v_i(t)$ . The Fourier transformation can be

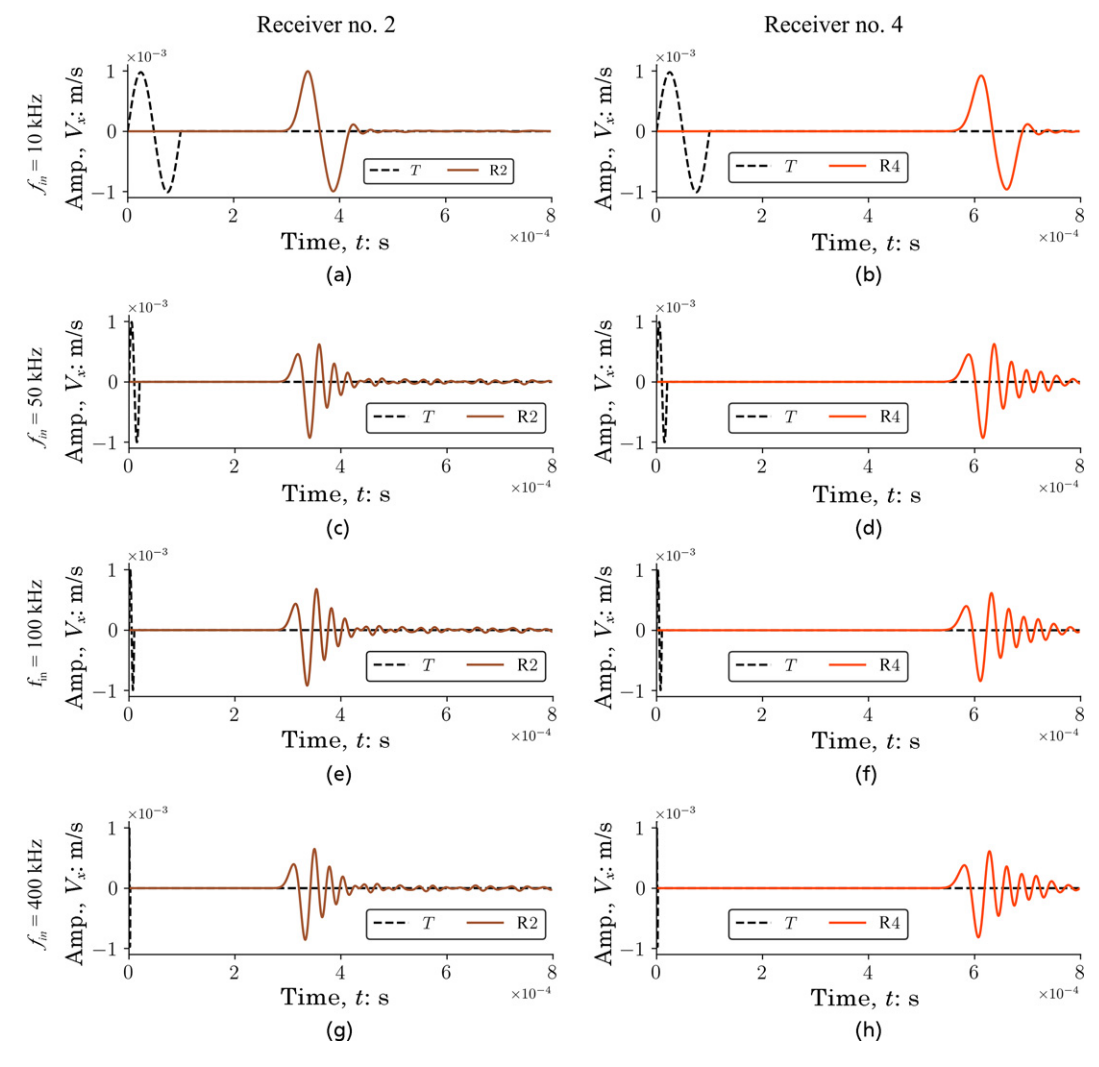


Fig. 4. The effect of input frequencies on received waveforms of shear wave test for a FC-0 sample (e=0.540, p=100 kPa).  $\zeta$  denotes the amplification factor that magnifies the amplitude of output signals: (a) R2,  $f_{in}=10$  kHz,  $\zeta=1.0$ ; (b) R4,  $f_{in}=10$  kHz,  $\zeta=1.0$ ; (c) R2,  $f_{in}=50$  kHz,  $\zeta=2.0$ ; (d) R4,  $f_{in}=50$  kHz,  $\zeta=2.0$ ; (e) R2,  $f_{in}=100$  kHz,  $\zeta=7.0$ ; (f) R4,  $f_{in}=100$  kHz,  $\zeta=10.0$ ; (g) R2,  $f_{in}=400$  kHz,  $\zeta=10.0$ ; (h) R4,  $f_{in}=400$  kHz,  $\zeta=150.0$ 

operated from time domain to wavenumber domain by way of a position vector, which is expressed as:

$$v_k = \sum_{i=1}^{N} v_i(t) e^{-Ikx_i t}$$
 (12)

where I is the imaginary unit and k is the wave vector. Next the second Fourier transformation is operated from time domain to frequency domain as:

$$\mathbf{v}_k(\omega) = \int_0^\infty \mathbf{v}_k(t)e^{I\omega t} \mathrm{d}t \tag{13}$$

which produces the power spectrum of the particle velocity  $\chi = |\mathbf{v}_k(\omega)|^2$ . The long-wavelength velocity can be determined from the peak branch of the dispersion relation on the condition of  $\lim_{k\to 0} \omega/k$ . It should be mentioned that both compression (P-) wave and shear (S-) wave tests have been performed for all the elongated samples and only S-wave simulation results are used to analyse the wave behaviour in the following content. As illustrated in Fig. 5, the attenuation is observed to be more severe across the frequency content as the input frequency increases from 10 to 400 Hz. The vibrational density of states (vDoS) is usually used to investigate the sample responses upon varying frequencies. Just as 2D FFT, the vDoS is readily obtained as (Cheng *et al.*, 2020; Tang & Yang, 2021):

$$D(\omega) = \sum_{k}^{N_k d_k} \chi(k, \omega) \Delta k \tag{14}$$

where  $d_k$  and  $N_k$  are the minimum and maximum wavenumbers defined by the packing length and particle size. In other words, the replication number and associated sample dimension determines the accuracy of both dispersion relation and vDoS.

#### RESULTS AND DISCUSSION

Wave behaviour in granular media with fines

To understand the effect of FC on wave propagation, three specific samples with varying FC (i.e. 0, 2.5 and 5%) are prepared with the void ratio close to 0.540 under the isotropic confining pressure of 100 kPa. The samples are labelled as FC-0-T1, FC-2.5-T2 and FC-5-T3, respectively, and the associated information is summarised in Table 3. From the post-processing images shown in Fig. 6, it is intuitive to observe that shear waves propagate at varying speeds and the profiles of the planar-like wave fronts are notably different through the granular samples with varying FC. The received wave signals at receiver 3 (R3) are plotted in Fig. 7 to exhibit the difference in time domain. It is noted that  $V_s$  determined by peak-to-peak method on the

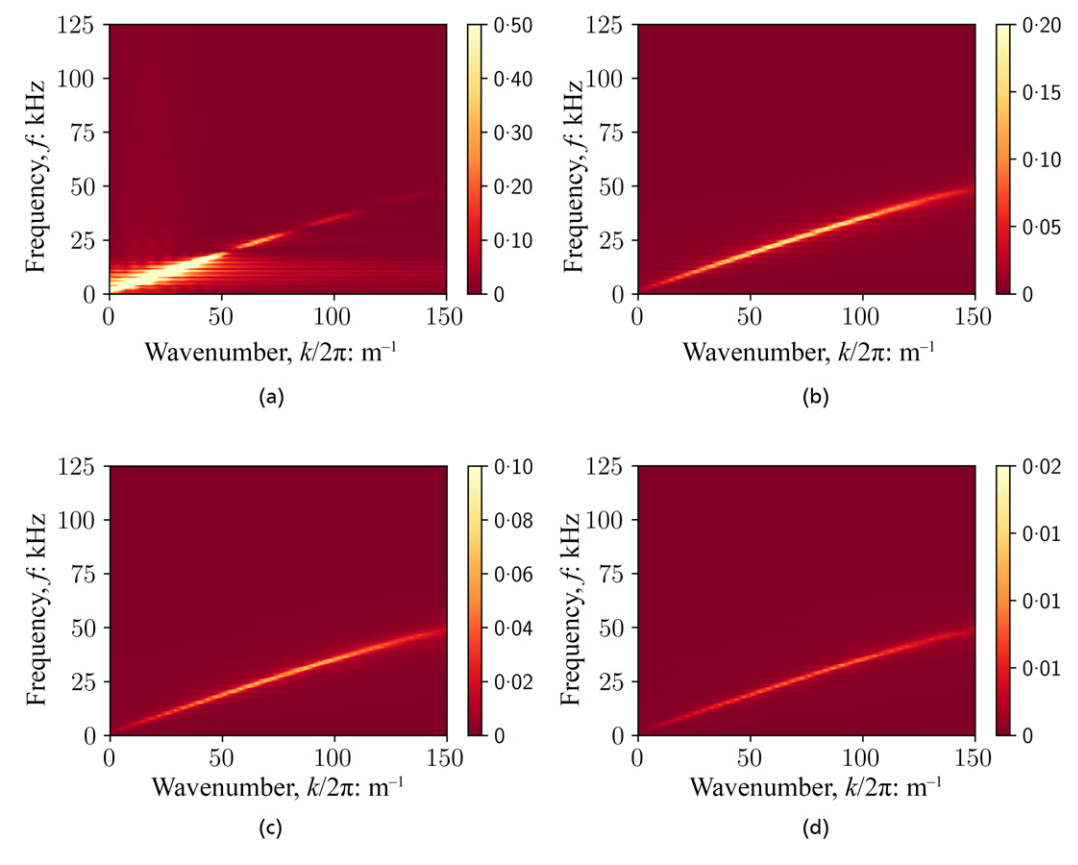


Fig. 5. The effect of input frequencies on dispersion relations of shear wave test for a FC-0 sample (e = 0.540, p = 100 kPa): (a)  $f_{in} = 10$  kHz; (b)  $f_{in} = 50$  kHz; (c)  $f_{in} = 100$  kHz; (d)  $f_{in} = 400$  kHz

Table 3. Comparison test series concerning the fines content (FC) effect

Sample ID	е	Z	$Z_M$	<i>V<sub>s</sub></i> : m/s
FC-0-T1	0·523	5·479	6·057	357·730
FC-2·5-T2	0·524	2·684	5·705	339·090
FC-5-T3	0·523	1·650	5·125	304·850

time-domain signal is used for the following discussion. The arrival of the first peak is delayed as FC increases and the shear wave velocity decreases from 357.73 m/s to  $304\cdot85\,\text{m/s}.$  The amplitude of the first peak decreases approximately from  $5\cdot0\,\times\,10^{-5}$  m/s to  $2\cdot0\,\times\,10^{-5}$  m/s, which indicates a higher damping mechanism directly attributed to higher FC. In addition to time domain, the transmission of frequency spectrums can be generated to explore the evolution of the wave frequency content. As plotted in the middle column of Fig. 7, it can be observed that the sharp reduction occurs immediately after the wave propagation and the distance is about 20 times the mean particle size (that is  $20D_{50}$ ). Also, it can be identified that the cut-off frequency,  $f_{cut}$ , decreases from around 39.3 to 21.9 kHz, accompanied by a prominent reduction in amplitudes for the overall frequency range. Having observed the considerable effect of FC, it is important to uncover the micromechanical insights on wave propagation. The conventional coordination number is defined as  $Z = 2N_c/N_p$ , where  $N_c$  is the number of contacts and  $N_p$  is the number of particles. As highlighted in Gu & Yang (2013), the mechanical coordination number is more effective in characterising the elastic properties of granular materials, which is expressed as in Thornton (2000):

$$Z_M = \frac{2N_c - N_p^1}{N_p - \left(N_p^0 + N_p^1\right)} \tag{15}$$

where  $N_p^0$  denotes the number of particles without any contact, and  $N_p^1$  refers to the number of particles with only one contact. As listed in Table 3, both Z and  $Z_M$  decrease while the difference between Z and  $Z_M$  increases as FC increases up to 5%, which implies that a higher FC is associated with a higher percentage of rattlers that are not effectively involved in the contact network. As shown in Fig. 8, the inhomogeneity of the force chain network increases as the FC increases. In spite of the uniformity variations of contact force distribution, a great linear correlation can be identified between  $V_s$  and  $Z_M$  as  $V_s = 59.31Z_M$ . When it comes to cut-off frequency, it is also clear that  $f_{cut}$  and  $Z_M$  can be linearly correlated as

$$f_{cut} = 18 \cdot 20Z_M - 71 \cdot 60 \tag{16}$$

Both from post-processing images and wave analyses, it is found that the propagated wave signal is strongly linked with the effective contact numbers. It is also observed from Fig. 6 that the chaotic oscillation is stronger as FC increases, which supports the findings that the scattering phase is mainly influenced by the internal contact network (Jia, 2004). Bassett *et al.* (2012) carried a 2D sound propagation test on photo-elastic nodes and suggested that the scattering phase can be better predicted by local structures. Further numerical investigation will be helpful to eludicate how the configuration of contact network affects the wave scattering.

In order to isolate the effect of FC, in total, four samples are prepared based on FC = 2.5%, including FC-2.5-T1 under the isotropic confining pressure of 100 kPa. In

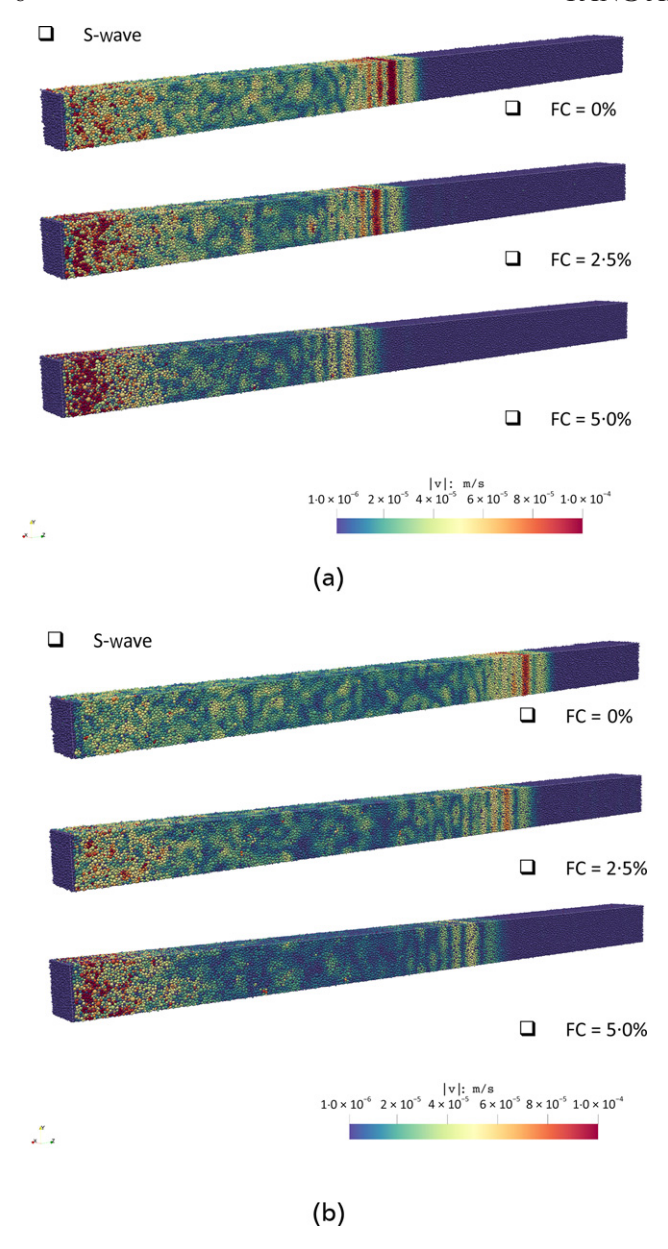


Fig. 6. Post-process visualisations of shear wave propagation in the elongated specimens with different fines content (FC) but similar post-consolidation state ( $e \approx 0.523$ , p = 100 kPa): (a) elapsed propagation time at  $4.0 \times 10^{-4}$  s; (b) elapsed propagation time at  $6.0 \times 10^{-4}$  s

particular, the post-consolidation void ratio varies from 0.499 to 0.568 covering the dense state to the loose state of this spherical granular material in DEM; these are labelled FC-2·5-T0, T1, T2 and T3. Dispersion relations of shear waves in specimens of FC-2.5 with different void ratios at the isotropic confining pressure of 100 kPa are: (a) FC-2·5-T0, e = 0.499; (b) FC-2·5-T2, e = 0.559; (c) FC-2·5-T3, e = 0.568. As shown in Fig. 9, it is notable that the highlighted bright colours faded from a dense to a loose state, which represents the peak values of the 2D Fourier transformation graphs. Furthermore, it is evident that much more high-frequency content has been filtered out in the loose sample referring to the horizontal and vertical axes. It is also clear that the overall amplitude of the power spectrum drops as the void ratio increases, which indicates a higher attenuation effect. In particular, the peak value of FC-2·5-T3 is around five times smaller than that of FC-2·5-T0, which can be explained by the obvious smaller  $Z_M$ . These are very good examples demonstrating

how the states of specimens can significantly affect the dispersive behaviour of granular media.

Having addressed the effect of void ratio, it is also interesting to discover the effect on confining stress as the elevation of stress level can enhance the overall efficiency of the contact network, which is commonly represented in different empirical formulas. A very loose sample, namely FC-2·5-IC100, is prepared with the void ratio of 0.592 at the isotropic confining pressure of 100 kPa. Then the sample is further consolidated up to 5000 kPa and in total three states are used here for discussion, namely, FC-2·5-IC100, IC2000 and IC5000. As can be directly seen from Fig. 10, it is obvious that the peak branches have generally higher maximum amplitudes and rotate anti-clockwise as the confining pressure increases. The anti-clockwise rotation intuitively indicates the increase of group velocity. Also, more frequency content can be found to transit through the assembly along with the elevated stress levels. In particular, the cut-off frequency,  $f_{cut}$ , increases from about 25 to 70 kHz. Therefore, not only wave velocity but also the transmitted frequency spectrum is altered as the isotropic stress levels grows. With these findings, it is understood that either the effective contact number or the average contact force can notably affect the wave speed, attenuation and filtering.

Cross-scale characterisation of shear wave velocities

As mentioned earlier, several hundreds of wave propagation tests are performed to generate a systematic dataset in terms of FC, void ratio and confining stress. As shown in Fig. 11, the shear wave velocities are plotted against void ratio for each material from low to high confining stresses. The general trend is well supported by the laboratory test results by Yang & Liu (2016): that is, under otherwise similar conditions,  $V_s$  decreases as the FC increases. From the classic equation (Hardin & Richart, 1963), shear wave velocities can be predicted by the void ratio, e, and the corresponding mean effective stress, p, which is conventionally expressed as:

$$V_s = \alpha_s (B_s - e) p^{\beta_s} \tag{17}$$

where the subscript s denotes the shear wave;  $B_s$ ,  $\alpha_s$  and  $\beta_s$ are fitting parameters. After fitting the shear wave velocities, for each type of material with a certain FC, the fitted  $B_s$  values vary slightly with varying stress levels. Within 5% FC,  $B_s$  is approximately the same and drops to 0.75 when the FC increases up to 10%. The  $\alpha_s$  value is observed to decrease from 335.073 to 283.793 as the FC increases up to 5%, and then suddenly rises up to 456·148. The fitting parameters are listed for samples with varying FC in Table 4. Referring to Fig. 12(a), there are good relationships between  $V_s/f(e)$  and p for materials with varying FC where  $f(e) = B_s - e$ . It is clear that no unique relationship can be identified if FC significantly varies. Similar observations can also be obtained from laboratory tests on Toyoura sand mixed with different amounts of fines (Yang et al., 2018). It appears from Fig. 12(a) that there is a turning point between FC-5 and FC-10. The reason for the observed turning point is that the void ratio range of DEM specimens tends to shift towards the smaller side with increasing FC, as shown in Fig. 12(b), and this void ratio difference will affect the void ratio function f(e). If the stress-normalised shear wave velocities  $V_{s1}$  are plotted against e, where  $V_{s1} = V_s(p_a/p)^{1/6}$ , it becomes clear that, for a given e,  $V_{s1}$  is smaller as the FC is higher, suggesting that the effect of FC is continuous and there is no transitional behaviour for the range of FC. Future work to expand the

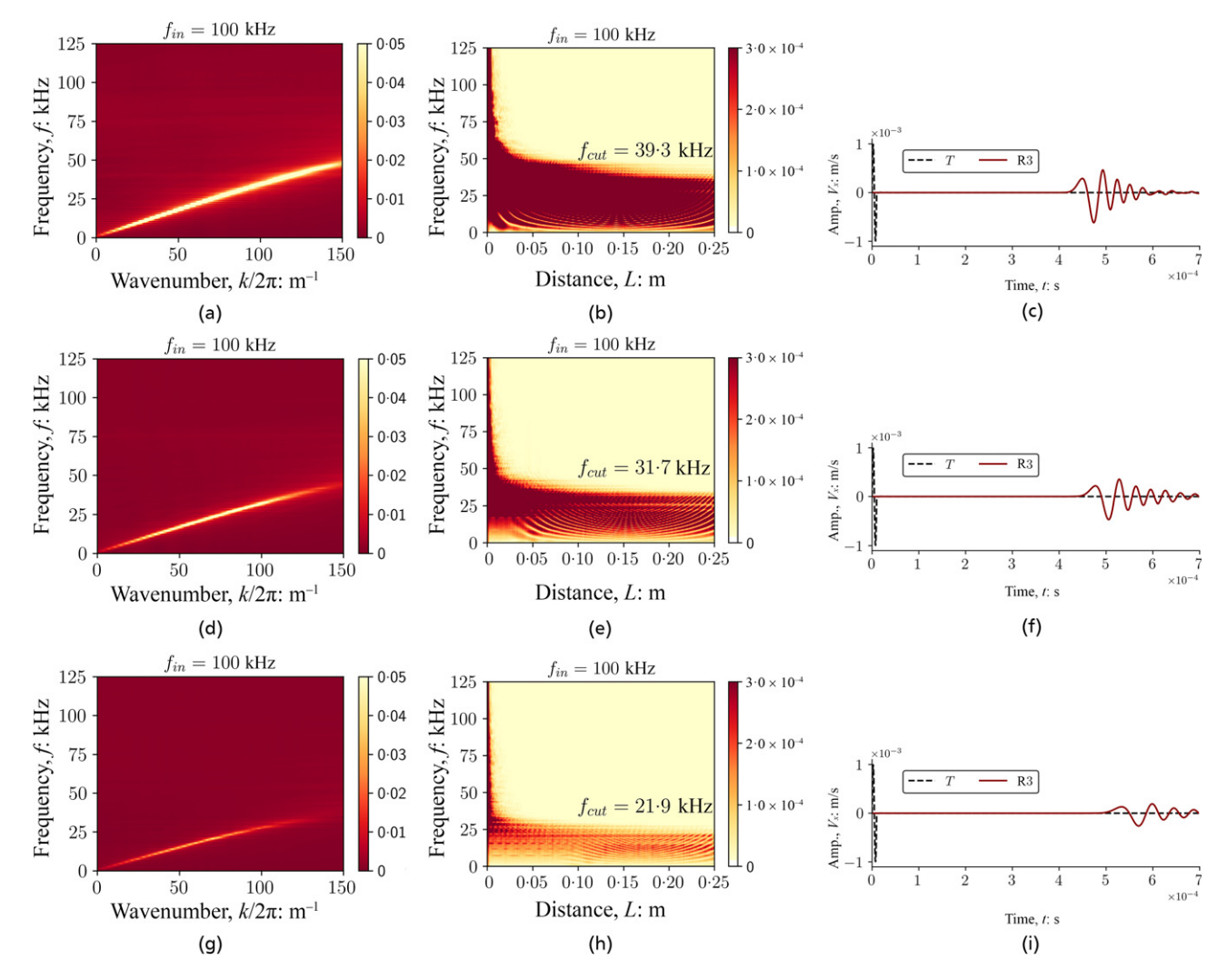


Fig. 7. Comparison on dispersion relation, frequency spectrum transmission and time-domain signals of shear waves for materials with varying FC at similar state ( $e \approx 0.523$ , p = 100 kPa): (a), (b), (c) FC-0-T1; (d), (e), (f) FC-2.5-T2; (g), (h), (i) FC-5-T3

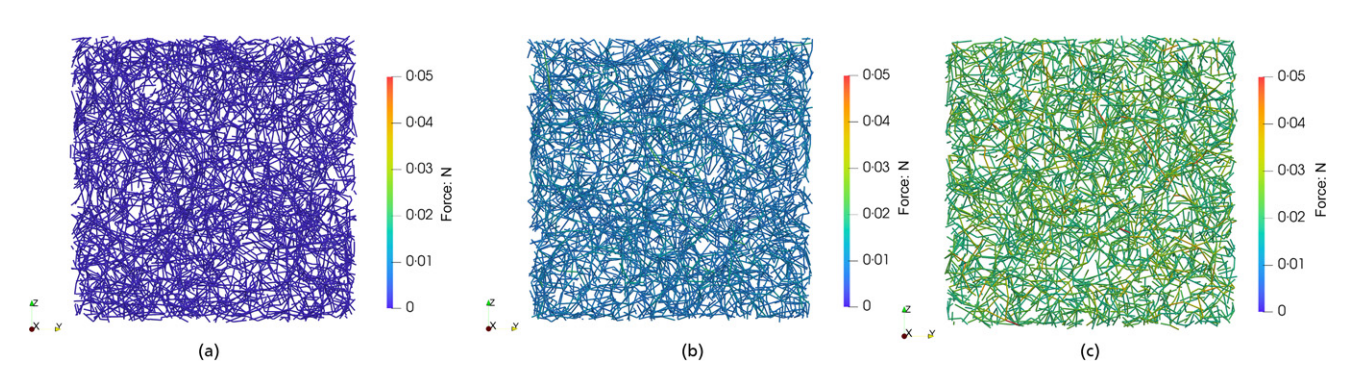


Fig. 8. Cross-sections of contact force network of specimens with varying FC at similar states ( $e \approx 0.523$ , p = 100 kPa): (a) FC-0-T1; (b) FC-2·5-T2; (c) FC-5-T3

present study from a low percentage to a high percentage (Wichtmann *et al.*, 2015; Lopera Perez *et al.*, 2016) would be of interest.

As an alternative density index for sand-fines mixtures, equivalent void ratio (or intergranular void ratio) has received increasing attention (Thevanayagam & Martin, 2002; Ni *et al.*, 2004; Rahman *et al.*, 2008; Lashkari, 2014). By assuming a certain amount of fines participates in the force transmission of sand-fines mixtures, the equivalent skeleton void ratio,  $e^*$ , is defined as

$$e^* = \frac{e + (1 - b)FC}{1 - (1 - b)FC}$$
 (18)

where b stands for the portion of fines that are involved in force transmission inside sand–fines mixtures. Based on the definition, b shall vary between 0 and 1. When b=0, the intergranular void ratio shrinks to the so-called skeleton void ratio that assumes no FC takes part in transferring forces. Often the b value is determined by an empirical formula (Rahman *et al.*, 2008) or back-analysis of test data

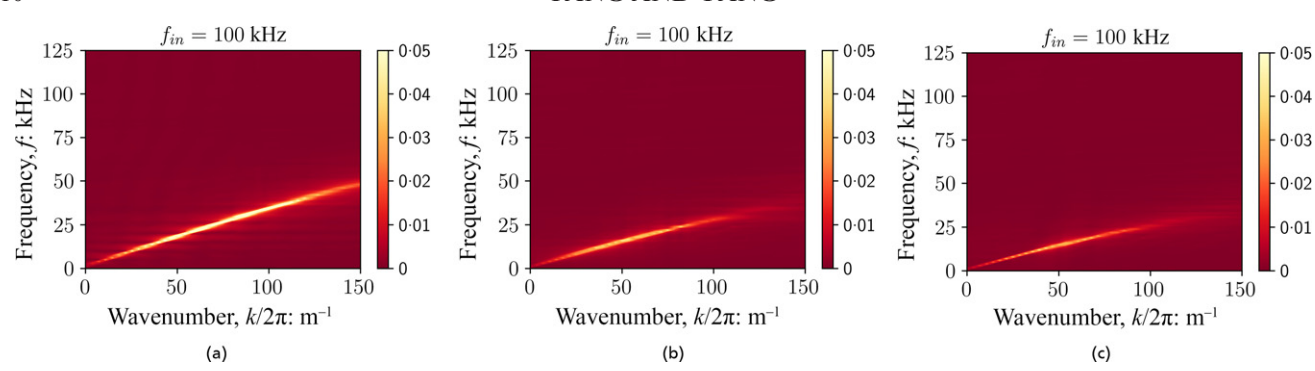


Fig. 9. Dispersion relations of shear waves in specimens of FC-2·5 with different void ratios at p=100 kPa: (a) FC-2·5-T0, e=0.499; (b) FC-2·5-T2, e=0.559; (c) FC-2·5-T3, e=0.568

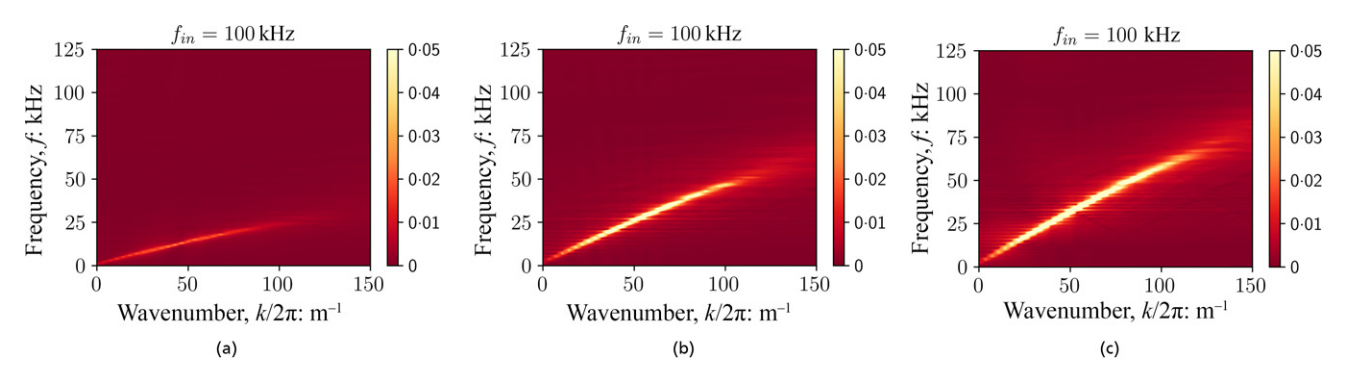


Fig. 10. Dispersion relations of shear waves in specimens of FC-2·5-IC100 (e = 0.592, p = 100 kPa) with elevated stress levels: (a) FC-2·5-IC100; (b) FC-2·5-IC2000 (c) FC-2·5-IC5000

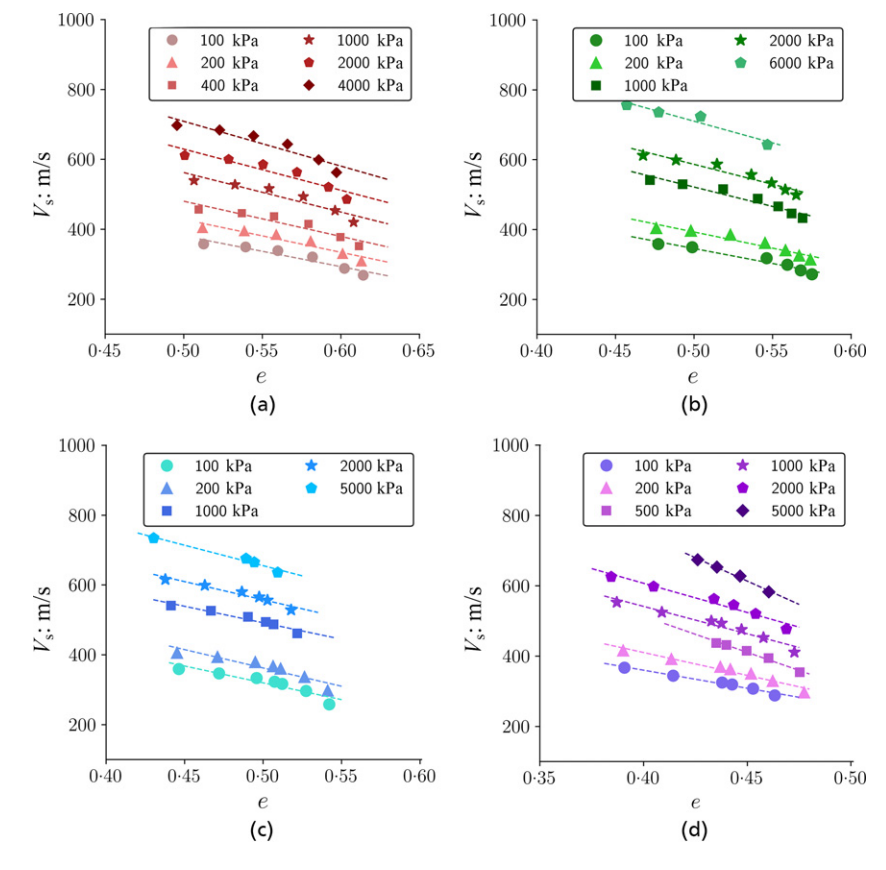


Fig. 11. Relationship between shear wave velocity  $V_s$  and void ratio e for specimens with varying fines content (FC) at different mean effective stresses: (a) FC-0; (b) FC-2·5; (c) FC-5; (d) FC-10

Table 4. Fitting parameters for characterising the shear wave velocities with varying FC

Material	$B_{s}$	$\alpha_s$	$\beta_s$
FC-0	1·001	335·073	0·175
FC-2·5	0·977	322·546	0·176
FC-5	0·991	283·793	0·182
FC-10	0·750	456·148	0·176

(Thevanayagam et al., 2002; Ni et al., 2004). Recently, the equivalent void ratio has been extended to the equivalent state parameter (Lashkari, 2014; Rahman & Lo, 2014). While the idea appears to be appealing, care should be used as the calculated b values may not always bear the physical meaning assumed, as shown by particle-level simulations of sand–fines mixtures (Luo & Yang, 2013) and by the backanalysis of different datasets of sand–fines mixtures in the literature (Lashkari, 2014). It was also noted that the behaviour of sand–fines mixtures may not be necessarily unified by simply using the equivalent skeleton void ratio (Carrera et al., 2011; Yang et al., 2015). This inconsistency is not surprising since intergranular contacts of mixed soils are highly complex and depend on many factors, including particle characteristics (Yang et al., 2015; Wei & Yang, 2023).

In an elastic medium, the shear wave is transmitted in bulk matter that is equal to the square root of the ratio of shear modulus and density as expressed as  $V_s = \sqrt{G_0/\rho_d}$ ,

where  $G_0$  is the shear modulus at small strain and  $\rho_d$  is the dry sample density. The effective medium theory (EMT) has been commonly employed to characterise and predict the elastic properties of homogenised granular solids (Chang *et al.*, 1995), which fundamentally connects the macroscopic elastic properties and microscopic parameters at small strain. From the EMT theory, for a given p, the relationship between wave velocities and microscopic parameters can be proposed as

$$V_s \sim Z_M^{1/3} e^{-1/3} p^{1/6} \tag{19}$$

where  $V_s$  refers to the shear wave velocity;  $Z_M$  is the mechanical coordination number; and e is the void ratio under the mean effective stress p. At constant void ratio and mean effective stress, it is clear that the  $Z_M$  is observed to be smaller if the FC increases (see Fig. 13(a)). To isolate the effect of confining stresses, a fairly good relationship can be identified between the stress-normalised  $V_{s1}$  and  $Z_M^{1/3}$ , as demonstrated in Fig. 13(b). Similarly, the macroscopic small-strain shear modulus and microscopic average contact number can be expected based on

$$G_0 \sim \left(\frac{Z_M}{1+e}\right)^{2/3} p^{1/3}$$
 (20)

The micromechanical approach is physically intuitive as it reflects the compound effect of effective connectivity and force magnitude of the contact network inside the granular media.

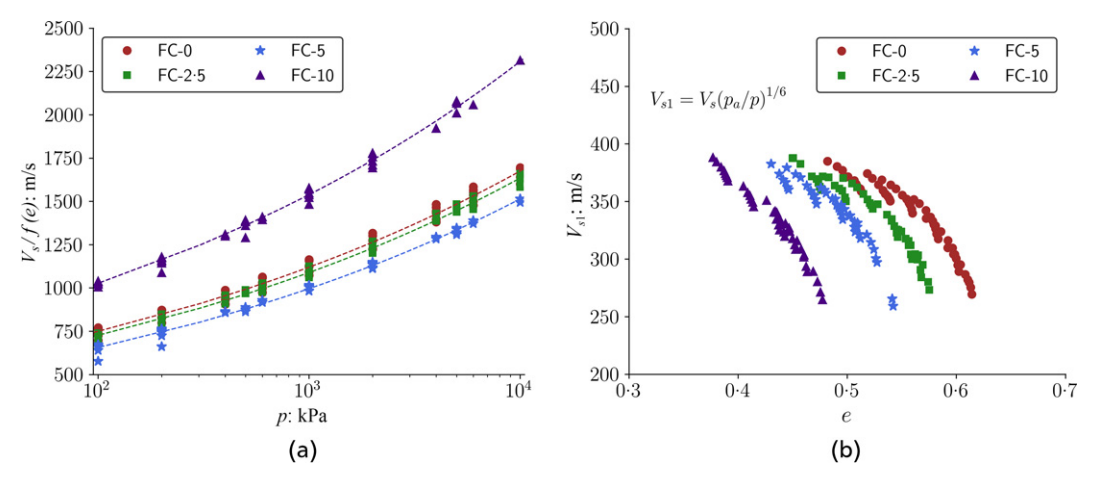


Fig. 12. Characterisation of  $V_s$  by conventional approach: (a)  $V_s If(e)$  plotted against p; (b)  $V_{s1}$  plotted against e

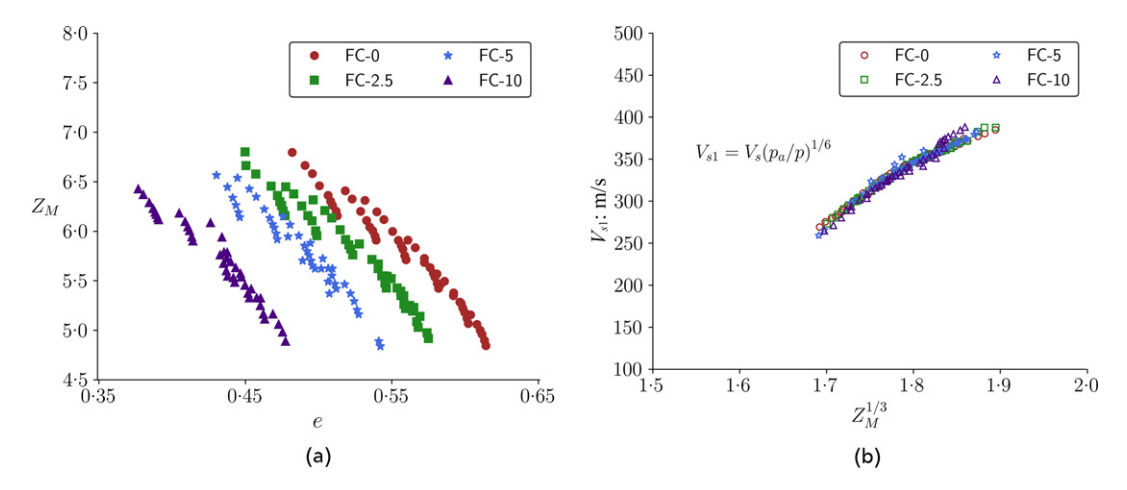


Fig. 13. Micromechanical characterisation of elastic wave velocities and associated shear modulus with presence of varying fines content (FC): (a)  $Z_M$  plotted against e; (b)  $Vs_1$  plotted against  $Z_M^{1/3}$ 

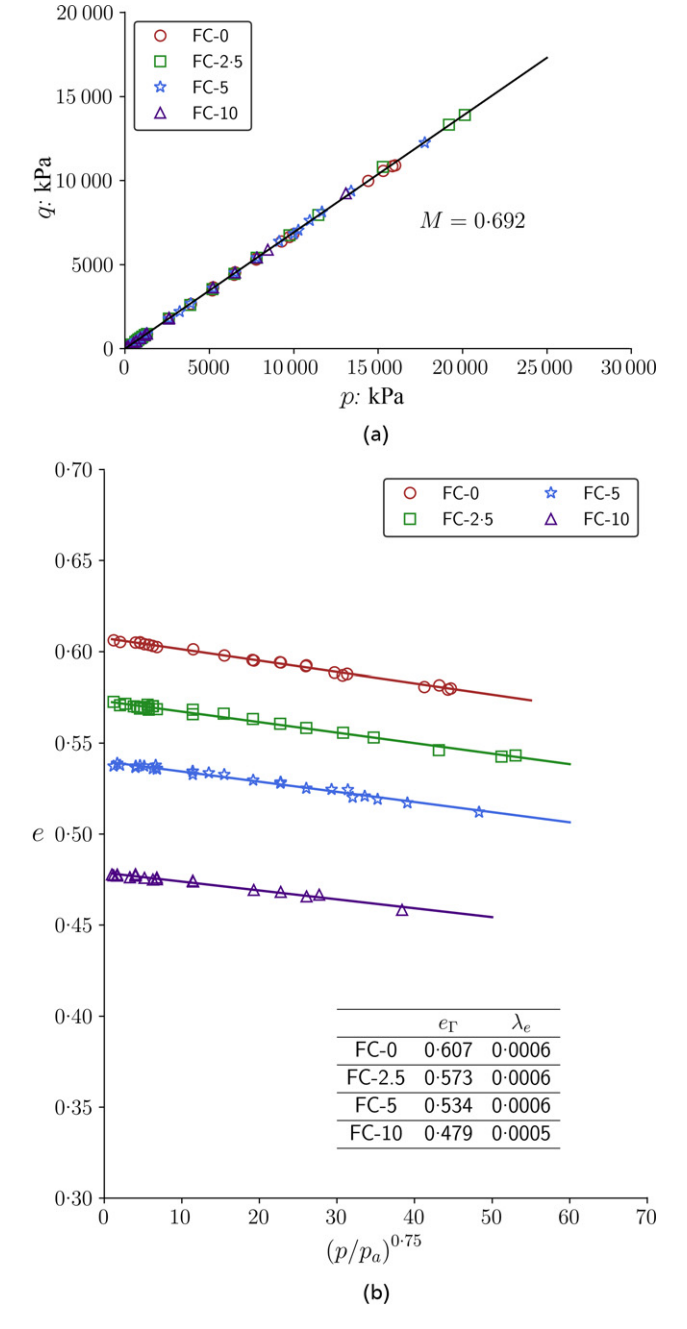


Fig. 14. Critical state lines for varying fines content (FC) from series of triaxial tests: (a) CSL in q-p plane; (b) CSL in e-p plane

Characterisation of wave velocities by unified framework under critical state soil mechanics

Based on the principles of unified framework, there are two types of tests required to characterise the shear wave velocities by state parameter. In this study, triaxial tests are numerically modelled on the exact same RVEs that are purposely modified for wave propagation. Particularly, more than 100 triaxial tests are performed to establish reliable critical state lines. Often, it is convenient to characterise the critical state by projecting the status into two planes as expressed as:

$$q = Mp (21)$$

$$e = e_{cs} = e\Gamma - \lambda_e \left(\frac{p}{p_a}\right)^{\xi_e} \tag{22}$$

where  $e_{\Gamma}$  is usually taken as the void ratio intercepting at p = 0, and  $\lambda_e$  refers to the slope of the straight critical state line. It should be mentioned that the optimised  $\xi_e$  is found to be 0.75, so different from the 0.60 that has been widely used in extensive laboratory testing results (Yang et al., 2018). As illustrated in Fig. 14(a), it seems that the critical friction angle seems not to be affected by varying FC. In particular, a constant M is identified as 0.692 at critical state, and the critical state friction angle  $\varphi_{cs}$  is 18.07°, which is well matched by the prediction of Yang & Luo (2015). As for critical state characteristics in the e-p plane shown in Fig. 14(b), the critical state locus (CSL) is observed to shift downwards clearly. Referring to equations (21) & (22), the critical state parameters are summarised in the inset plot of Fig. 14(b), which clearly indicates that  $e_{\Gamma}$ decreases from 0.607 to 0.479. The parameter  $\lambda_e$  seems not to be changed based on the stress exponent  $\xi_e = 0.75$ . The current simulation results are generally matched with the laboratory testing results on Toyoura sand mixed with crushed silica fines (Yang et al., 2018).

Once the CSL is known, the state parameter for the wave test sample can be obtained by referring the initial state to the critical state. It is noted that most of the samples tend to be located at the dense side, probably because only spherical particles are adopted under dry conditions. For each wave test specimen, its state parameter can be determined as  $\Psi = e - e_{cs}$ , where e denotes the current void ratio and  $e_{cs}$  is the critical state void ratio (Been & Jefferies, 1985). If all data points of  $V_s$  are plotted here in Fig. 15(a), no unique relationship exists between the two quantities concerned. And if the shear wave velocity is normalised by the stress, it exhibits a fairly good relationship between  $V_{s1}$ 

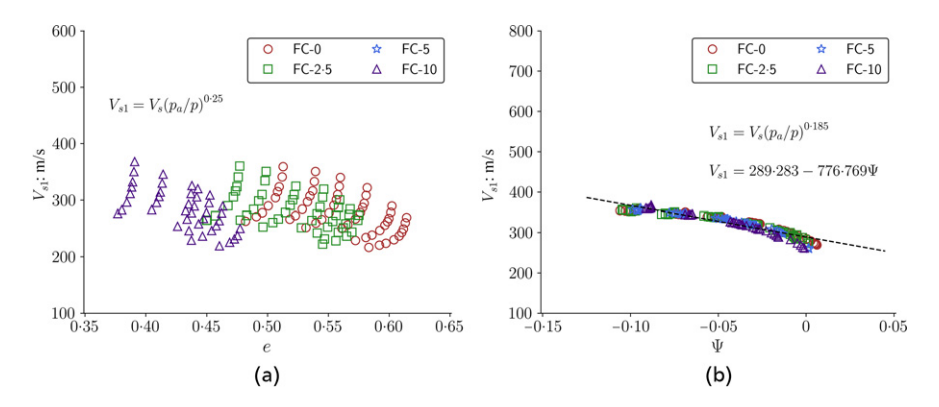


Fig. 15. Characterisation of stress-normalised shear wave velocities of materials with varying fines content (FC) by different methods: (a)  $V_{s1}$  plotted against e; (b)  $V_{s1}$  plotted against  $\Psi$ 

and  $\Psi$ , other than scattering points (see Fig. 15(b)). The corresponding relation can be expressed as

$$V_{s1} = V_s(p_a/p)^n = \mathbf{A} - \mathbf{B}\Psi \tag{23}$$

where A, B and n are material constants dependent on particle characteristics. From the DEM results here, they are determined as 289·28 m/s, 776·77 m/s and 0·185. The significance of Equation (23) is that it represents a unified relationship connecting  $V_{s1}$  and  $\Psi$  for both clean and silty sands, in which  $\Psi$  is a rational state variable to characterise mechanical behaviour under both monotonic and cyclic loading conditions (Yang, 2024). Along with laboratory experiments (Yang et al., 2018), the particle-level simulation results here lend good support to such a unified relationship and provide insights into the microscopic mechanism. Its application in soil liquefaction evaluation has been demonstrated to be rather appealing (Yang, 2024).

# SUMMARY AND CONCLUSIONS

Elastic wave propagation in granular media is one of the most fundamental problems in mechanics and physics, having both scientific fascination and practical importance across many disciplines. This paper presents a novel study that is aimed at exploring the role of fine particles in altering elastic wave propagation, including both wave velocity and the frequency spectrum in granular media. Different approaches to characterise the shear wave velocities of granular materials with varying FC are examined. The main results and findings are summarised below.

- (a) For a given initial state in terms of void ratio and confining stress, the shear wave velocity reduces with increasing FC. Meanwhile, it is found that much more high-frequency content is filtered and the damping effect becomes notably higher during the propagation process in granular media with higher FC. The associated features of wave propagation can be well correlated to the effective contact numbers other than the homogeneity degree of the contact network.
- (b) Based on a broad range of simulation results, it is observed that the range of void ratio generally shifts towards smaller values as the FC increases, which results in difficulties when characterising the wave velocities for granular assemblies mixed with fines. At the particulate level, the coordination number decreases as the FC increases for a given reference state. It is also found that there are higher percentage of rattlers and less effective contacts as the FC increases. Based on the EMT theory, a sound relationship is found between the mechanical coordination number and the stress-normalised shear wave velocity.
- (c) Based on the numerical triaxial tests conducted on similar granular assemblies, it is found that the critical state friction angle is not sensitive to the presence of fines, but the critical state line on the e-p plane shifts downwards as the FC increases. Given the systematic simulation data, it becomes convincing that the scattered data points observed in the V<sub>s</sub>-e plot can be resolved by replacing e with ψ, which firmly supports that the unified framework, developed from recent laboratory experiments (Yang & Liu, 2016; Yang et al., 2018), is able to characterise the shear wave velocity of granular materials regardless of FC in a simple yet rational way.

#### **ACKNOWLEDGEMENTS**

The financial support provided by the Research Grants Council (RGC) of Hong Kong (nos. 17207923; C7038-20G; N-HKU723/23) is gratefully acknowledged. The computations were performed using high-performance computing facilities offered by the Information Technology Service (ITS) of the University of Hong Kong (HKU).

# **NOTATION**

 $B_s$ ,  $\alpha_s$ ,  $\beta_s$  fitting parameters of shear wave velocities

**d**<sup>c</sup> branch vector

e global void ratio (ratio between volume of void

space and volume of solids)

e\* equivalent skeleton void ratio or intergranular void

 $e_{cs}$  critical state void ratio

 $e_{\Gamma}$  void ratio intercept for critical state line in power-

law form

 $f^c$  contact force tensor

 $f_{cut}$  cut-off frequency

 $f_{in}$  input frequency

 $f_n$  contact normal force

 $f_t$  contact tangential force

 $f_{\rm vd}$  relative velocity based viscous damping force

G<sub>0</sub> small-strain shear modulus

 $H_i$  cell dimensions

L inertia number

M effective stress ratio at the critical state

 $N_n^0$ ,  $N_n^1$  number of particles with zero and one contact,

respectively

 $N_c$ ,  $N_p$  number of contacts and number of particles

p hydrostatic stress or mean effective stress in triaxial

 $p_a$  reference atmosphere pressure

q deviatoric stress in triaxial test

 $V_s$  shear wave velocity

 $V_{s1}$  stress-normalised shear wave velocity

v particle velocity

 $Z, Z_M$  coordination number and mechanical coordination number

γ<sub>vel</sub> velocity damping coefficient

 $\delta_n$  contact normal overlap

 $\delta_t$  relative tangential displacement

 $\varepsilon_i$  cell average strain tensor

 $\mu$  interparticle friction coefficient

 $\rho_d$  dry sample density

 $\rho_g$  particle grain density

 $\sigma$  cell stress tensor

Ψ state parameter

# REFERENCES

Alshibli, K. A., Batiste, S. N. & Sture, S. (2003). Strain localization in sand: plane strain versus triaxial compression. J. Geotech. Geoenviron. Engng 129, No. 6, 483–494.

Bassett, D. S., Owens, E. T., Daniels, K. E. & Porter, M. A. (2012). Influence of network topology on sound propagation in granular materials. *Phys. Rev. E Stat. Nonlin. Soft Matter Phys.* 86, No. 4 Pt 1, 041306, https://doi.org/10.1103/PhysRevE.86.041306.

Been, K. & Jefferies, M. G. (1985). A state parameter for sands. *Géotechnique* **35**, No. 2, 99–112.

Carrera, A., Coop, M. & Lancellotta, R. (2011). Influence of grading on the mechanical behaviour of stava tailings. *Géotechnique* 61, No. 11, 935–946, https://doi.org/10.1680/geot.9.P.009.

Chang, C. S., Chao, S. J. & Chang, Y. (1995). Estimates of elastic moduli for granular material with anisotropic random packing structure. *Int. J. Solids Structs* 32, No. 14, 1989–2008, https:// doi.org/10.1016/0020-7683(94)00225-L.

Cheng, H., Luding, S., Saitoh, K. & Magnanimo, V. (2020). Elastic wave propagation in dry granular media: effects of

- probing characteristics and stress history. *Int. J. Solids Structs* **187**, 85–99, https://doi.org/10.1016/j.ijsolstr.2019.03.030.
- Chien, L. K. & Oh, Y. N. (2002). Influence of fines content and initial shear stress on dynamic properties of hydraulic reclaimed soil. *Can. Geotech. J.* 39, No. 1, 242–253, https:// doi.org/10.1139/t01-082.
- Choo, H. & Burns, S. E. (2015). Shear wave velocity of granular mixtures of silica particles as a function of finer fraction, size ratios and void ratios. *Granul. Matter* 17, No. 5, 567–578, https://doi.org/10.1007/s10035-015-0580-2.
- Christoffersen, J., Mehrabadi, M. M. & Nemat-Nasser, S. (1981). A micromechanical description of granular material behavior. J. Appl. Mech. 48, No. 2, 339–344, https://doi.org/ 10.1115/1.3157619.
- Cundall, P. A. (1988). Computer simulations of dense sphere assemblies. In *Micromechanics of granular materials* (eds M. Satake and J. T. Jenkins), pp. 113–123. Amsterdam: Elsevier.
- Cundall, P. A. & Strack, O. D. L. (1979). A discrete numerical model for granular assemblies. *Géotechnique* 29, No. 1, 47–65, https://doi.org/10.1680/geot.1979.29.1.47.
- Da Cruz, F., Emam, S., Prochnow, M., Roux, J.-N. & Chevoir, F. (2005). Rheophysics of dense granular materials: discrete simulation of plane shear flows. *Phys. Rev. E* 72, No. 2, 21309.
- Gollwitzer, F., Rehberg, I., Kruelle, C. A. & Huang, K. (2012). Coefficient of restitution for wet particles. *Phys. Rev. E Stat. Nonlin. Soft Matter Phys.* 86, No. 1 Pt 1, 011303, https://doi.org/10.1103/PhysRevE.86.011303.
- Gu, X. Q. & Yang, J. (2013). A discrete element analysis of elastic properties of granular materials. *Granul. Matter* 15, No. 2, 139–147, https://doi.org/10.1007/s10035-013-0390-3.
- Gu, X., Liang, X., Shan, Y., Huang, X. & Tessari, A. (2020). Discrete element modeling of shear wave propagation using bender elements in confined granular materials of different grain sizes. *Comput. Geotech.* 125, No. May, 103672, https://doi.org/10.1016/j.compgeo.2020.103672.
- Hardin, B. O. & Richart, F. E. Jr (1963). Elastic wave velocities in granular soils. J. Soil Mech. Found. Div. 89, No. 1, 33–65.
- Huang, X., O'sullivan, C., Hanley, K. J. & Kwok, C. Y. (2014). Discrete-element method analysis of the state parameter. *Géotechnique* 64, No. 12, 954–965, https://doi.org/10.1680/geot.14.p.013.
- Jia, X. (2004). Codalike multiple scattering of elastic waves in dense granular media. *Phys. Rev. Lett.* 93, No. 15, 154303–154311, https://doi.org/10.1103/PhysRevLett.93.154303.
- Johnson, K. L. (1985). Contact mechanics. Cambridge University Press. https://doi.org/10.1017/CBO9781139171731.
- Kloss, C., Goniva, C., Hager, A., Amberger, S. & Pirker, S. (2012). Models, algorithms and validation for opensource DEM and CFD-DEM. Prog. Comput. Fluid Dyn. Int. J. 12, No. 2–3, 140–152.
- Kuerbis, R., Negussey, D. & Vaid, Y. P. (1988). Effect of gradation and fines content on the undrained response of sand. Geotech. Special Publication 21, 330–345.
- Lade, P. V. & Yamamuro, J. A. (1997). Effects of nonplastic fines on static liquefaction of sands. *Can. Geotech. J.* 34, No. 6, 918–928.
- Lade, P. V., Liggio, C. D. & Yamamuro, J. A. (1998). Effects of non-plastic fines on minimum and maximum void ratios of sand. *Geotech. Testing J.* 21, No. 4, 336–347, https://doi.org/ 10.1520/gtj11373j.
- Lashkari, A. (2014). Recommendations for extension and recalibration of an existing sand constitutive model taking into account varying non-plastic fines content. *Soil Dyn. Earthq. Engng* 61–62, 212–238, https://doi.org/10.1016/j. soildyn.2014.02.012.
- Li, X. S. & Dafalias, Y. F. (2012). Anisotropic critical state theory: role of fabric. *J. Engng Mech.* 138, No. 3, 263–275, https://doi.org/10.1061/(asce)em.1943-7889.0000324.
- Liu, X. & Yang, J. (2018). Shear wave velocity in sand: effect of grain shape. Géotechnique 68, No. 8, 742–748, https://doi. org/10.1680/jgeot.17.T.011.
- Liu, D., O'Sullivan, C. & Carraro, J. A. H. (2023). The influence of particle size distribution on the stress distribution in granular materials. *Géotechnique* **73**, No. 3, 250–264, https://doi.org/10.1680/jgeot.21.00127.

- Lopera Perez, J. C., Kwok, C. Y., O'Sullivan, C., Huang, X. & Hanley, K. J. (2016). Assessing the quasi-static conditions for shearing in granular media within the critical state soil mechanics framework. Soils Found. 56, No. 1, 152–159.
- Luo, X. & Yang, J. (2013). Effects of fines on shear behavior of sand: a DEM analysis. In *Proceedings of 5th international* young geotechnical engineers' conference, Paris, France, pp. 265–268. https://doi.org/10.3233/978-1-61499-297-4-265.
- Mouraille, O. & Luding, S. (2008). Sound wave propagation in weakly polydisperse granular materials. *Ultrasonics* **48**, No. 6–7, 498–505, https://doi.org/10.1016/j.ultras.2008.03.009.
- Murthy, T. G., Loukidis, D., Carraro, J. A. H., Prezzi, M. & Salgado, R. (2007). Undrained monotonic response of clean and silty sands. *Géotechnique* 57, No. 3, 273–288.
- Ni, Q., Tan, T. S., Dasari, G. R. & Hight, D. W. (2004). Contribution of fines to the compressive strength of mixed soils. *Géotechnique* 54, No. 9, 561–569, https://doi.org/ 10.1680/geot.54.9.561.56936.
- Ning, Z., Khoubani, A. & Evans, T. M. (2015). Shear wave propagation in granular assemblies. *Comput. Geotech.* **69**, 615–626, https://doi.org/10.1016/j.compgeo.2015.07.004.
- O'Donovan, J., O'Sullivan, C., Marketos, G. & Muir Wood, D. (2015). Analysis of bender element test interpretation using the discrete element method. *Granul. Matter* 17, No. 2, 197–216, https://doi.org/10.1007/s10035-015-0552-6.
- Oda, M. (1982). Fabric tensor for discontinuous geological materials. Soils Found. 22, No. 4, 96–108, https://doi.org/ 10.3208/sandf1972.22.4\_96.
- Otsubo, M., O'Sullivan, C., Hanley, K. J. & Sim, W. W. (2017). The influence of particle surface roughness on elastic stiffness and dynamic response. *Géotechnique* 67, No. 5, 452–459, https://doi.org/10.1680/jgeot.16.P.050.
- Rahman, M. M., Lo, S. R. & Gnanendran, C. T. (2008). On equivalent granular void ratio and steady state behaviour of loose sand with fines. *Can. Geotech. J.* 45, No. 10, 1439–1456, https://doi.org/10.1139/T08-064.
- Rahman, M. M. & Lo, S. R. (2014). Undrained behaviour of sand-fines mixtures and their state parameters. J. Geotech. Geoenviron. Engng 140, No. 7, 04014036.
- Rahman, M. M. & Lo, S. R. (2008). The prediction of equivalent granular steady state line of loose sand with fines. *Geomechanics and Geoengineering* **3** No. 3, 179–190, https://doi.org/10.1080/17486020802206867.
- Saitoh, K., Shrivastava, R. K. & Luding, S. (2019). Rotational sound in disordered granular materials. *Phys. Rev. E* 99, No. 1–1, 012906, https://doi.org/10.1103/PhysRevE.99.012906.
- Salgado, R., Bandini, P. & Karim, A. (2000). Shear strength and stiffness of silty sand. J. Geotech. Geoenviron. Engng 126, No. 5, 451–462.
- Shire, T. & O'Sullivan, C. (2016). Constriction size distributions of granular filters: a numerical study. *Géotechnique* **66**, No. 10, 826–839, https://doi.org/10.1680/jgeot.15.P.215.
- Somfai, E., Roux, J. N., Snoeijer, J. H., Van Hecke, M. & Van Saarloos, W. (2005). Elastic wave propagation in confined granular systems. *Phys. Rev. E Stat. Nonlin. Soft Matter Phys.* 72, No. 2 Pt 1, 021301, https://doi.org/ 10.1103/PhysRevE.72.021301.
- Tang, X. & Yang, J. (2021). Wave propagation in granular material: what is the role of particle shape? J. Mech. Phys. Solids 157, 104605, https://doi.org/10.1016/j.jmps.2021.104605.
- Thevanayagam, S. & Martin, G. R. (2002). Liquefaction in silty soils screening and remediation issues. *Soil Dyn. Earthquake Eng* **22**, No. 9–12, 1035–1042, https://doi.org/10.1016/S0267-7261(02)00128-8.
- Thevanayagam, S., Shenthan, T., Mohan, S. & Liang, J. (2002). Undrained fragility of clean sands, silty sands, and sandy silts. *J. Geotech. Geoenviron. Engng* 128, No. 10, 849–859, https://doi.org/10.1061/(asce)1090-0241(2002)128:10(849).
- Thornton, C. (2000). Numerical simulations of deviatoric shear deformation of granular media. *Géotechnique* 50, No. 1, 43–53, https://doi.org/10.1680/geot.2000.50.1.43.
- Tsuji, Y., Kawaguchi, T. & Tanaka, T. (1993). Discrete particle simulation of two-dimensional fluidized bed. *Powder Technol.* 77, No. 1, 79–87.

- Wei, L. M. & Yang, J. (2014). On the role of grain shape in static liquefaction of sand-fines mixtures. Géotechnique 64, No. 9, 740-745, https://doi.org/10.1680/geot.14.T.013.
- Wei, X. & Yang, J. (2023). Characterising the effect of particle size disparity on liquefaction resistance of non-plastic silty sands from a critical state perspective. *Géotechnique* 73, No. 4, 323–336, https://doi.org/10.1680/jgeot.21.00145.
- Wichtmann, T., Navarrete Hernández, M. A. & Triantafyllidis, T. (2015). On the influence of a non-cohesive fines content on small strain stiffness, modulus degradation and damping of quartz sand. Soil Dyn. Earthq. Engng 69, No. 2, 103–114, https://doi.org/10.1016/j.soildyn.2014.10.017.
- Yamashita, S., Kawaguchi, T., Nakata, Y., Mikami, T., Fujiwara, T. & Shibuya, S. (2009). Interpretation of international parallel test on the measurement of *G*<sub>max</sub> using bender elements. *Soils Found.* **49**, No. 4, 631–650, https://doi.org/10.3208/sandf.49.631.
- Yang, J. (2024). Towards a novel method for liquefaction evaluation of silty sands. *JGS Special Publication* **10**, No. 5, 96–107, https://doi.org/10.3208/jgssp.v10.KL-2-02.
- Yang, J. & Gu, X. Q. (2013). Shear stiffness of granular material at small strains: does it depend on grain size? Géotechnique 63, No. 2, 165–179, https://doi.org/10.1680/ geot.11.P.083.
- Yang, J. & Liu, X. (2016). Shear wave velocity and stiffness of sand: the role of non-plastic fines. *Géotechnique* **66**, No. 6, 500–514, https://doi.org/10.1680/jgeot.15.P.205.

- Yang, J. & Luo, X. D. (2015). Exploring the relationship between critical state and particle shape for granular materials. J. Mech. Phys. Solids 84, 196–213, https://doi.org/ 10.1016/j.jmps.2015.08.001.
- Yang, J. & Wei, L. M. (2012). Collapse of loose sand with the addition of fines: the role of particle shape. *Géotechnique* 62, No. 12, 1111–1125, https://doi.org/10.1680/geot.11.P.062.
- Yang, J., Wei, L. M. & Dai, B. B. (2015). State variables for silty sands: Global void ratio or skeleton void ratio? Soils Found. 55, No. 1, 99–111, https://doi.org/10.1016/j. sandf.2014.12.008.
- Yang, J., Liu, X., Guo, Y. & Liang, L. B. (2018). A unified framework for evaluating in situ state of sand with varying fines content. *Géotechnique* 68, No. 2, 177–183, https://doi. org/10.1680/jgeot.16.P.254.
- Zhai, C., Herbold, E. B. & Hurley, R. C. (2020). The influence of packing structure and interparticle forces on ultrasound transmission in granular media. *Proc. Natn Acad. Sci. USA* 117, No. 28, 16234–16242, https://doi.org/10.1073/pnas.2004356117.
- Zlatović, S. & Ishihara, K. (1995). On the influence of nonplastic fines on residual strength. *First international conference on earthquake geotechnical engineering* **95**, 239–244.
- Zunker, W. & Kamrin, K. (2024). A mechanically-derived contact model for adhesive elastic-perfectly plastic particles, part I: Utilizing the method of dimensionality reduction. J. Mech. Phys. Solids 183, 105492, https://doi.org/10.1016/j. jmps.2023.105492.